Supplementary

Ultrahigh-quality graphene resonators by liquid-based strain-engineering

Ding-Rui Chen[a,b,c‡], I-Fan Hu[a,d‡], Hao-Ting Chin[a,b,c] Yu-Chi Yao[a,d], Radha Raman[b,c,e], Mario Hofmann[d], Chi-Te Liang[d]*, Ya-Ping Hsieh[a]*

[a]*Institute of Atomic and Molecular Sciences, Academia Sinica, Taipei 10617, Taiwan*

[b]*Department of Physics, National Taiwan University, Taipei 10617, Taiwan*

[c]*International Graduate Program of Molecular Science and Technology, National Taiwan University, Taipei 10617, Taiwan*

[d]*Molecular Science and Technology Program, Taiwan International Graduate Program, Academia Sinica, Taipei 10617, Taiwan*

[e]*Department of Physics, National Central University, Taoyuan 320, Taiwan*

‡*These authors contributed equally*

*Corresponding author Email: ctliang@phys.ntu.edu.tw and yphsieh@gate.sinica.edu.tw

Materials and Methods

1. Device layout

The graphene resonator array under consideration comprises numerous graphene resonators that are integrated within the graphene material itself. This arrangement has been achieved through the implementation of substrate-mediated strain engineering, as elucidated in the primary text. In order to serve as source and drain contacts, two contact electrodes (composed of silver paste) have been deposited at opposing ends of the device. The ensuing sections will delve into the discussion of three devised fabrication procedures aimed at evaluating the efficacy of the liquid tensioning process.

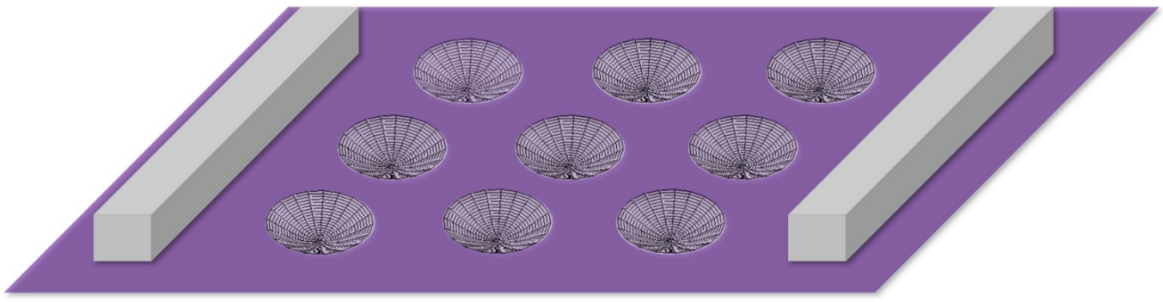

Figure S1 *A schematic of device layout*

2. Device fabrication

The fabrication methodology employed in this study is based on substrate-mediated strain

engineering of the graphene membrane. Liquid immersion is employed as a means to regulate the interaction between the graphene and the substrate. Through meticulous design of the substrate and the associated fabrication procedure, it becomes feasible to attain a resonator characterized by a notably high resonant frequency.

2.1 Substrate preparation

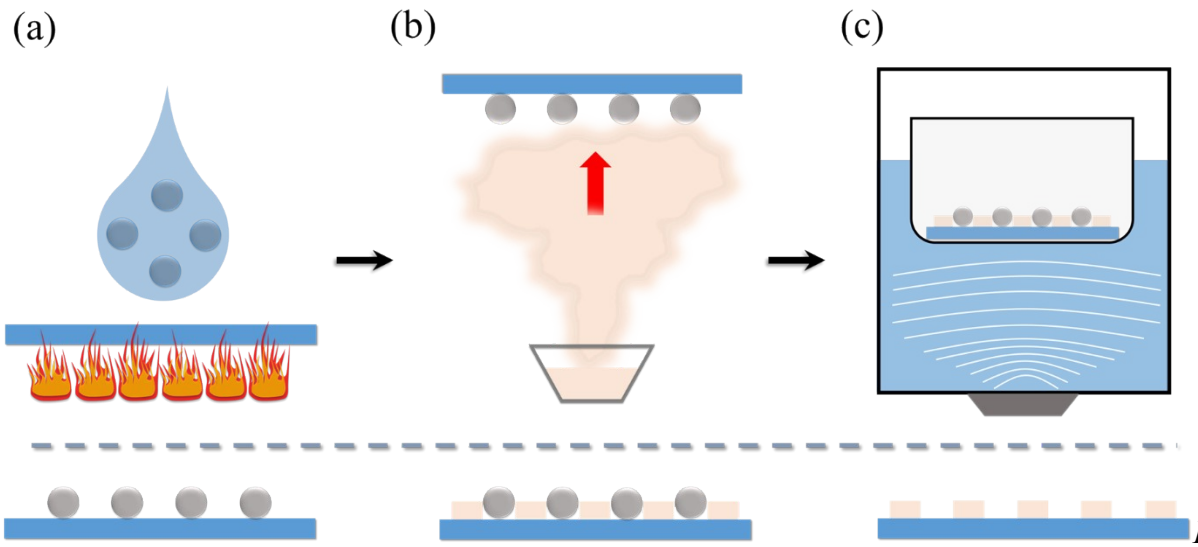

Figure S2 *Process of the nanosphere lithograpgy*

The substrate employed in this study was prepared using microsphere lithography, as depicted in ***Figure S2***. To achieve uniform distribution, microspheres were mixed in methanol and applied to a SiO_2/Si substrate (300 nm SiO_2) using the droplet evaporation technique. The volume ratio of microspheres to methanol solvent was set at 1:100. To stabilize the microsphere/methanol solvent mixture, a PMMA dilute solvent (diluted 50 times with methanol) was added.[1]

To enhance the hydrophilicity of the substrate, oxygen plasma treatment was carried out. During the droplet evaporation process, the substrate temperature was maintained at 393 K to ensure uniform evaporation and prohibit the formation of the coffee ring formation.[2] The droplet volume was precisely controlled using a pipette.

Following droplet evaporation, a 90 nm thick layer of alumina was deposited onto the microsphere-coated substrate using e-gun evaporation, with a deposition rate of 0.1 nm/s. Oxygen was introduced during the evaporation process to ensure the insulating properties of the alumina layer. Finally, the microspheres were removed via sonication, with a controlled power of 200 W to prevent any damage to the alumina layer.

Figure S3 illustrates optical microscope (OM) images of the well-separated hole array obtained after the removal of the microspheres. The average distance between two holes was found to be greater than 15 μm.

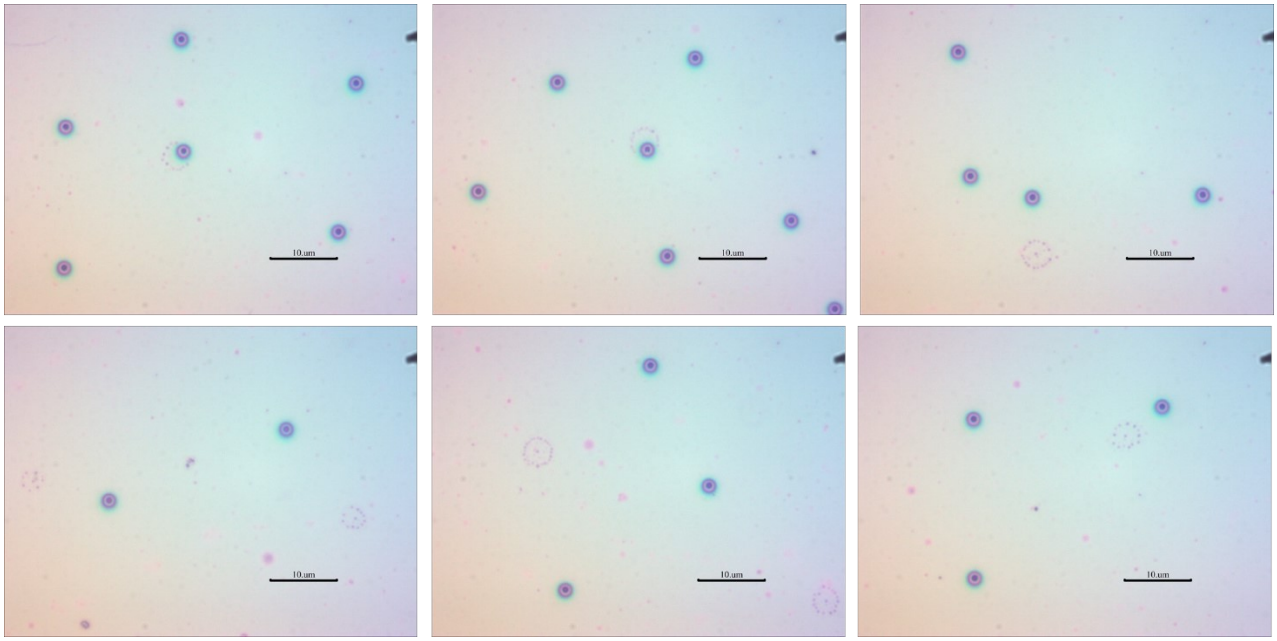

Figure S3 *Optical images for the as prepared substrate.*

2.2 Graphene growth

In this study, we employed the chemical vapor deposition (CVD) technique to synthesize graphene with the objective of achieving both centimeter-scale monolayer growth and transferability from the growth substrate. The process commenced with the electrochemical polishing of a copper foil at 1.5 V for a duration of 30 minutes, followed by annealing at 1020 °C for 70 minutes under a pressure of 10 Torr and a hydrogen flow rate of 10 sccm within a 1" quartz tube heated by a clamshell furnace. Subsequently, 10 sccm of methane gas was introduced to initiate graphene growth, with a growth duration of 10 hours. Finally, the sample was cooled to room temperature while maintaining a hydrogen flow rate of 10 sccm.

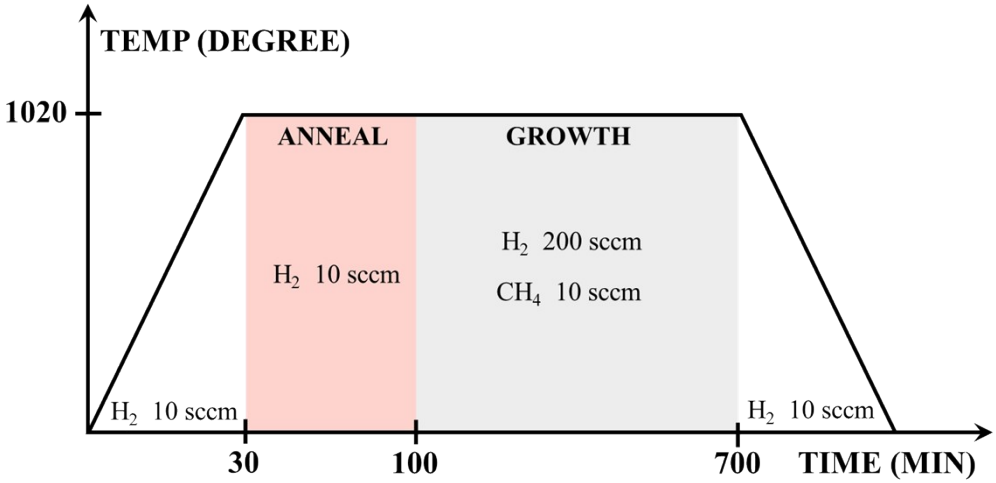

Figure S4 *Recipe of CVD graphene growth*

Figure S5 illustrates the Raman spectra obtained for the CVD graphene following its transfer onto a SiO_2/Si substrate using the wet-transferring process. The absence of the d-band in the Raman spectra indicates the exceptional quality of the graphene. Moreover, the mapping results provide further confirmation of the effectiveness of the CVD graphene synthesis procedure as depicted in ***Figure S4***.

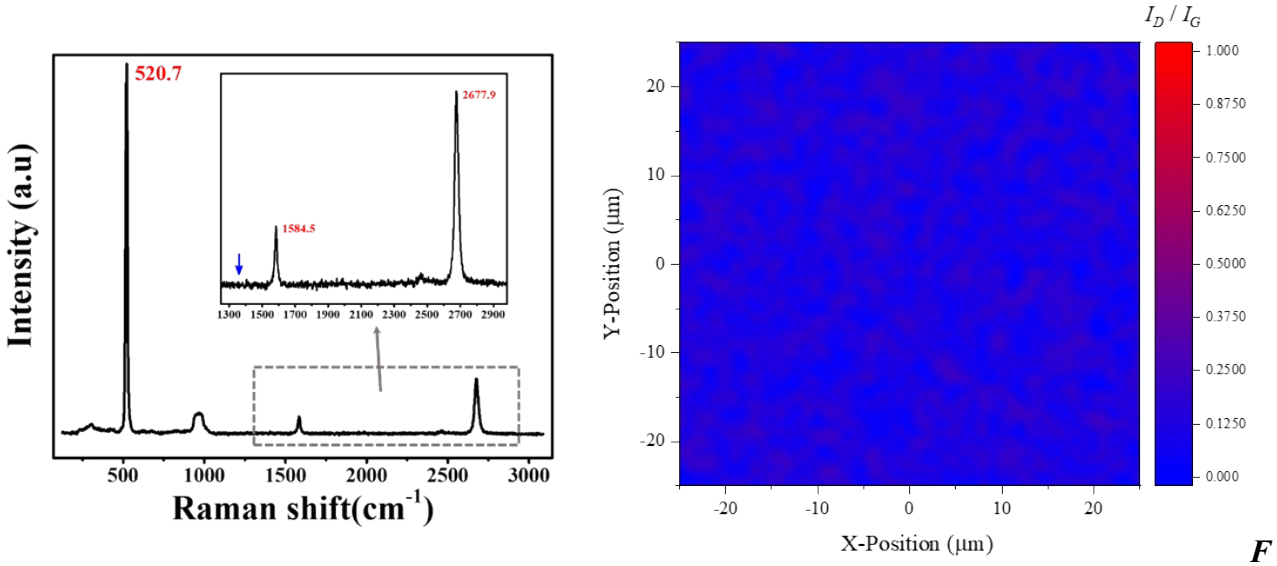

F

igure S5 *Raman spectra for the CVD graphene on SiO2*

2.3 Device fabrication

2.3.1 Procedure for water immersion

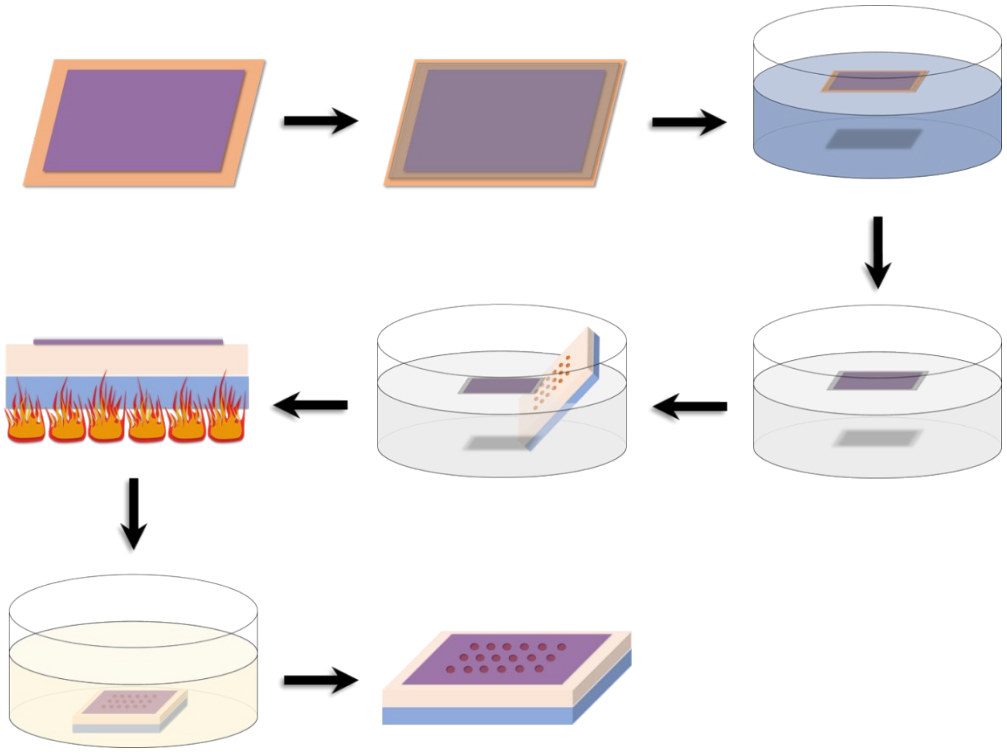

Figure S6 *Device fabrication procedure for the water immersion*

The present device fabrication protocol is specifically devised to incorporate an additional step involving water immersion.

1. Graphene is grown on a copper substrate through the CVD technique.
2. A layer of poly (methyl methacrylate) (PMMA) is applied as a coating onto the graphene-coated copper.
3. Copper etching is performed to selectively remove undesired regions.
4. Thorough removal of any residual etchant is ensured.
5. The PMMA/graphene layer is carefully collected.
6. The device is subjected to a baking process on a hot plate.
7. The PMMA layer is effectively eliminated by immersing the device in acetone.
8. The device is subsequently dried using a stream of nitrogen gas.

2.3.2 Procedure for acetone immersion

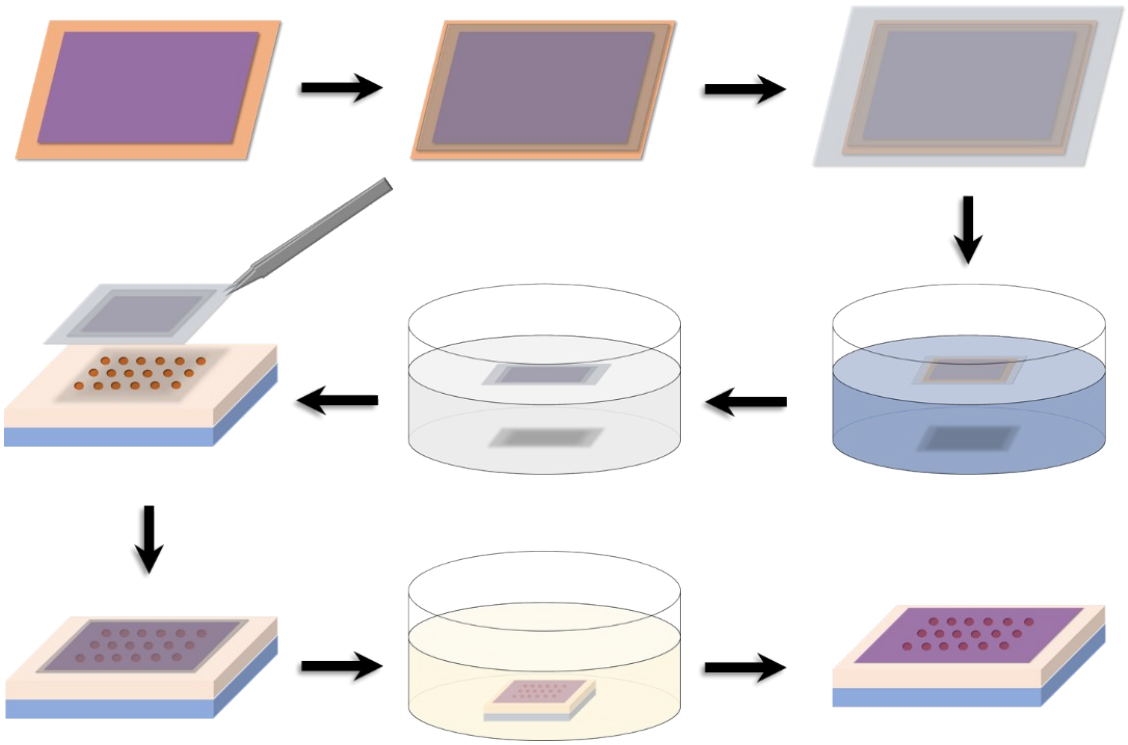

Figure S7 *Device fabrication procedure for acetone dipping*

Figure S7 Outlines a device fabrication protocol tailored for the production of resonator arrays, incorporating an additional step involving the immersion of the devices in acetone.

1. CVD technique is employed to grow a layer of graphene on a copper substrate.
2. A coating of PMMA is applied onto the graphene-coated copper.

3. A thermal release tape is then coated onto the PMMA layer.
4. Etching of the copper substrate is carried out, effectively removing the unwanted regions.
5. The remaining residue from the etching process is meticulously eliminated.
6. The resulting device is carefully transferred onto a pre-patterned substrate using a pair of tweezers.
7. The thermal release tape is subsequently removed from the device.
8. To remove the PMMA layer, the device is immersed in hot acetone at a temperature of 65°C.
9. The device is then dried using a stream of nitrogen gas.

2.3.3 Procedure for dry transferring

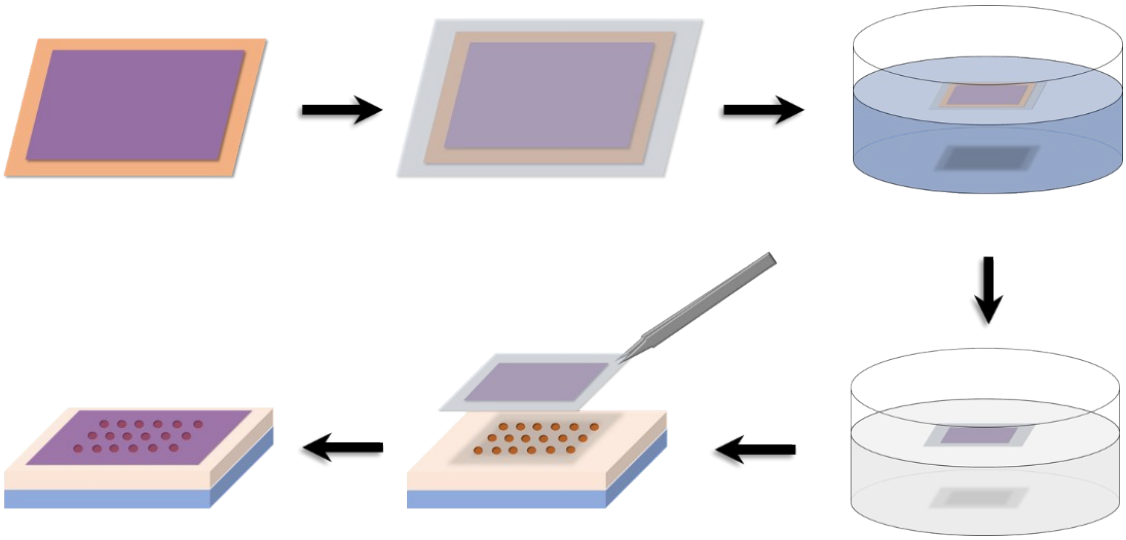

Figure S8 *Device fabrication procedure for the device without liquid immersion.*

The present methodology encompasses a device fabrication protocol tailored specifically for the construction of a resonator array in the absence of liquid immersion.

1. Synthesis of graphene on a copper substrate.
2. Application of thermal release tape as a protective coating.
3. Etching of the copper substrate.
4. Elimination of any residual etchant.
5. Precise transfer of the prepared graphene onto a substrate featuring a predefined pattern, utilizing tweezers.
6. Removal of the thermal release tape through a thermal release process.

3. Electrical measurements

3.1 Graphene field effect transistor (GFET)

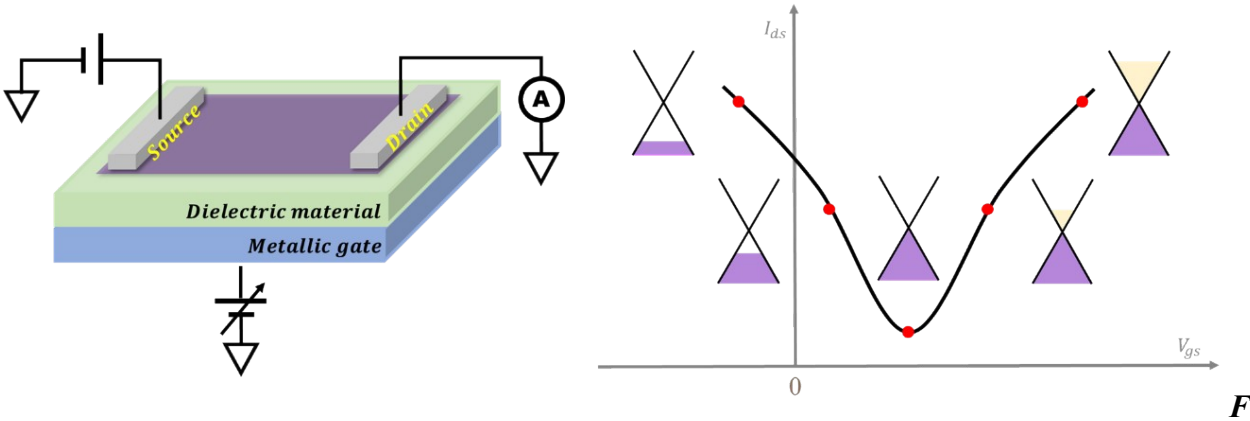

Figure S9 *A schematic of the GFET device structure and its corresponding transfer characteristic.*

The electrical read-out functionality of the array of graphene resonators relies on its gate-tunable conductivity, which arises from the low density of states near the Fermi level in graphene[3]. This characteristic of graphene lacking a band gap leads to a bi-polar conducting behavior, as demonstrated by the transfer curve depicted in ***Figure S9***.

3.2 Resonant frequency measurements

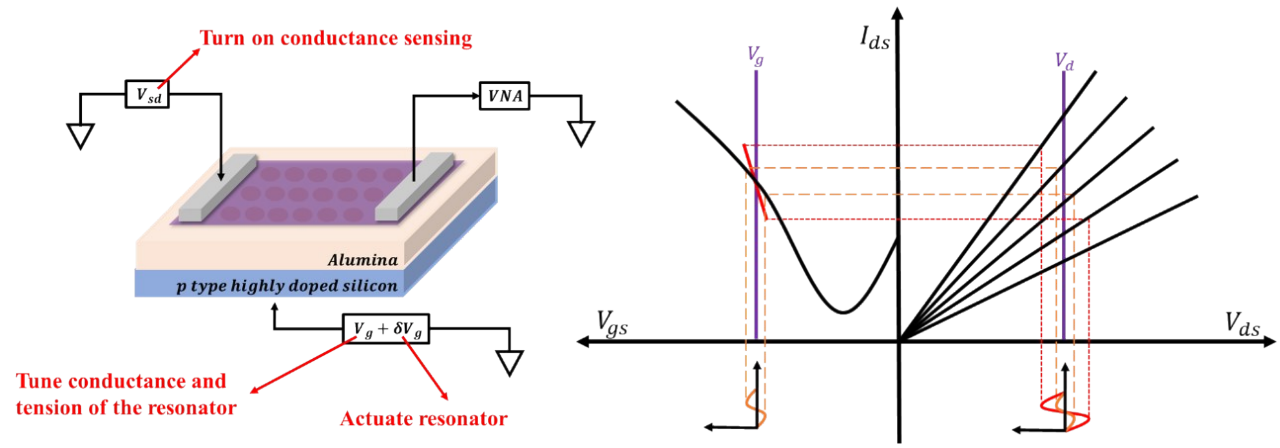

Figure S10 *Schematic diagrams for the combined actuation and sensing approach graphene resonators.*

The suspension of graphene enables the occurrence of out-of-plane motion in the graphene structure. By applying a voltage difference between the graphene and a gate, the suspended graphene undergoes deformation due to the capacitive force between the two. Consequently, the conductance of the graphene experiences changes as a result of variations in the effective field strength between the graphene and the gate. When an alternating electric field is applied to the graphene-gate system,

the capacitive force between them also becomes alternating, leading to the vibration of the graphene. This vibration, in turn, induces an alternative variation in conductance, as depicted in ***Figure S10***. The suspended graphene under this measurement technique is acted as a resonant channel (body) transistor.[4-5]

The amplitude of the alternative conductance is contingent upon the amplitude of the out-of-plane vibration in the graphene structure. Notably, the maximum vibration occurs when the suspended graphene film is driven by an alternating capacitive force with a frequency equal to the resonant frequency of the graphene. Consequently, by detecting the largest electrical response from the graphene resonator, one can determine its resonant frequency.

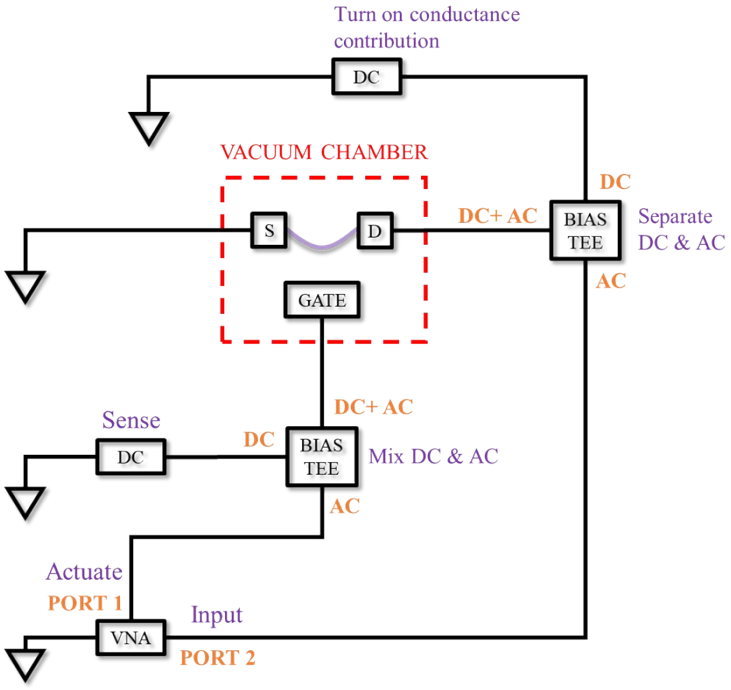

Figure S11 *Experimental setup for the electrical readout of the resonant frequency.*

The experimental setup is depicted in the ***Figure S11***. Our methodology closely followed a previous study,[6] wherein a vector network analyzer (VNA) was employed to manipulate and detect the graphene resonator array. A bias voltage originating from a DC power supply, along with an alternating voltage from the VNA, are combined using a bias-tee. This combined signal is then applied to the gate of the graphene resonator. The bias voltage serves the purpose of adjusting the conductance and tension of the resonator. Subsequently, the output signal from the resonator is fed into another bias-tee, which separates the AC and DC components. The AC signal is then directed to the VNA for further analysis.

Throughout the measurements, a direct current is passed through the source and drain contacts of the resonators in order to activate the conductance variation induced by vibration. It was observed that in the absence of this source-drain current, the resonant peak ceased to exist. This implies that within the dimensions of our device (1.5 μm), the changes in capacitance between the graphene and gate caused by vibration were not significant enough to be discerned in the output signal.

Consequently, it can be inferred that the variability in graphene's conductance is the primary contributing factor to the measurements of resonant frequency. Thus, the quality of the graphene material is of paramount importance in this particular experimental setup.

4. Tuneability comparison

Resonator	Tuning approach	Resonant frequency (MHz)	Tuning range (MHz)	Reference
Graphene resonator	Liquid tension	58	254	Our work
Bilayer beam resonator	Electrothermal tuning (Joule heating)	10.12	1.012	7
Nanotube resonator	Changing the length	300	30	8
Graphene resonator	Electrostatic tuning	52.19	5.219	9
Graphene resonator	Electrostatic tuning	51	4	9
Nanofiber resonator	Electrostatic spring-softening effect	0.58	0.058	10
Nanowire resonator	Electrostatic spring-softening effect	1.564	0.1564	11
Carbon-based nano-resonator	FIB-CVD machining	2.467	0.2467	12
Tungsten-based nano-resonator	FIB-CVD machining	1.352	0.1352	12
Tungsten-based nano-resonator	FIB-CVD machining	0.8532	0.08532	12
Cantilever nano-resonator	Bulk FIB machining	8.234	0.8234	13
Silicon nitride resonator	Dielectric actuation	6.5	0.65	14
Nanowire resonator	Electrostatic tuning	59	5.9	15
Nanotube resonator	Residual tension effect	9.44	0.944	16
Nanostring resonator	Tensile stress effect	9.3	0.93	17
CNTs resonator	Electrostatic softening effect	358.5	35.85	18
Graphene resonator	Electrostatic tuning	50	9	19
Graphene resonator	Electrostatic tuning	28	17	20

Table S1 *The detailed information for the comparison of tuneability.*

5. Frequency-dependent properties

5.1 Effect of imperfections

To address the question about the uniformity, we simulate the frequency response of different resonators using finite element methods. The simulation accurately captures the increase in fundamental frequency as the drum dimension decreases (Figure S12(a)).

We investigate the impact of defects on the resonator's performance by introducing interaction between neighboring membranes. A clear impact of resonator frequency for an increasing overlap can be observed (Figure S12(b)).

Finally, we characterize higher eigenmodes in defected resonators in dimer and trimer configurations. We observe characteristic differences in the fundamental end excited mode structure of such defects. However, the defected resonators exhibit higher order modes that overlap with the original resonance frequency (Figure S 12). The absence of such features in the experimental frequency plot indicates the suppression of such defects and the high quality of the employed resonators.

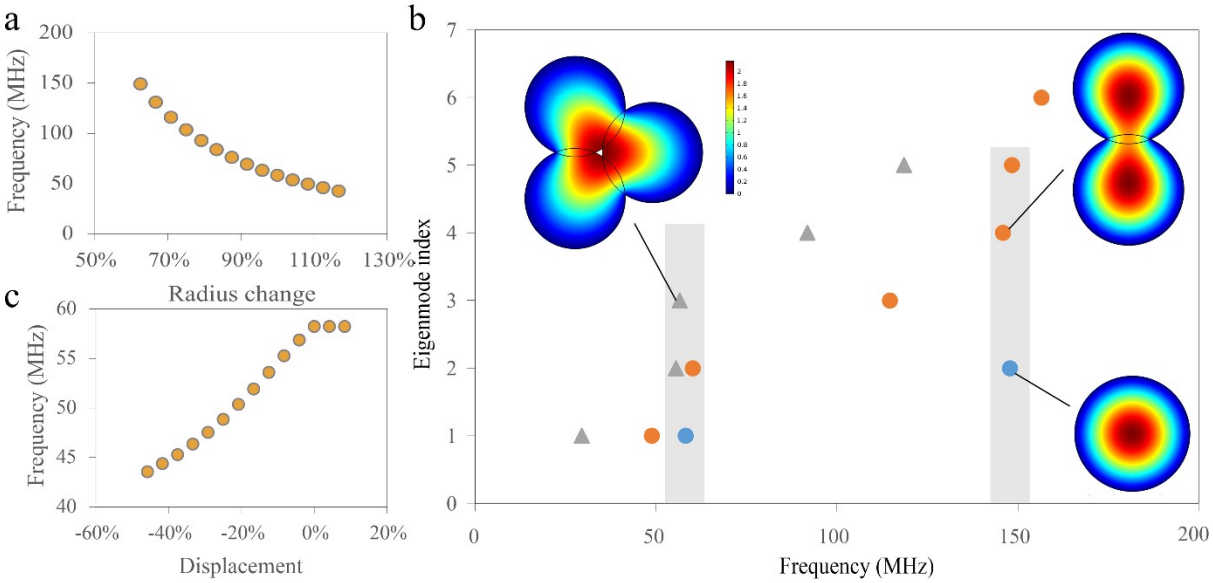

Figure S12 *Finite element simulation results on resonator morphology on properties (a) fundamental mode frequency as function of single drum dimension, (b) frequency contribution of different eigenmodes for three different resonator configurations: pristine single drum structures, dimer structures where membranes suspended over two neighboring holes are interacting, trimer structures where three membranes are interacting. The overlap of defect eigenmodes with the fundamental mode can be seen which is not observed in our experiments, (c) variation of fundamental eigenmode frequency as a function of dimer separation*

5.2 Effect of strain

The effect of strain on the resonance frequency can be modeled by a change of the effective spring constant K according to[21]

$$f_r = \frac{1}{2\pi}\sqrt{\frac{K}{m_{eff}}} = \frac{1}{2\pi}\sqrt{\frac{20.94Ew\left(\frac{d}{L}\right)^3 + 12.3\left(\frac{T}{L}\right)}{m_{eff}}} \quad \text{(equ. 1)}$$

, where L is the dimension of the resonator, T is the tension, E is the Young's modulus and d is the thickness of the membrane and m_{eff} is the membrane mass. A fit to this equation was provided in Figure 3(b).

5.3 Scaling analysis

We conduct a scaling analysis of the strain-dependent changes in quality factor to identify the mechanism that limits the performance of the resonator. A resonator's quality factor is determined by both intrinsic and extrinsic factors[22]

$$\frac{1}{Q_{tot}} = \frac{1}{Q_{int}} + \frac{1}{Q_{ext}} \quad \text{. (equ. 2)}$$

For external effects, we consider the energy loss due to incomplete clamping [23] which would limit the quality factor according to

$$Q_{clamp} \propto \frac{l}{w}\left(\frac{l}{t}\right)^4 \quad \text{(equ. 3)}$$

where l and w are the extents of the support and t is the resonator thickness.[24]
This behavior suggests that the dissipation rate scales linearly with resonant frequency according to[25]

$$\Gamma_{clamp} = \frac{\omega_r}{Q_{clamp}} = \omega_r \frac{w}{l}\left(\frac{t}{l}\right)^4 \quad \text{(equ. 3)}$$

Another source of energy loss could be viscous damping in air [Damping mechanisms of single-clamped and prestressed double-clamped resonant polymer microbeams]

$$\Gamma_{visc} = \frac{\omega_r}{Q_{intr}} = \frac{4}{\rho h}\sqrt{\frac{2M_m p}{RT}} \quad \text{(equ. 4)}$$

,where Mm is the mass of the gas molecules, p and T is the pressure and temperature of the gas.

From the equation, it can be seen that this dissipation is expected to be independent of resonant frequency and is thus a possible source of the observed damping.

Finally, the mechanical oscillation of carriers in the graphene induces a time-dependent potential in the gate which leads to friction and decoherence of the interacting electrons. [26] This behavior results in a frequency-independent loss rate according to

$$\Gamma_{decoh} = \frac{\hbar Q_C^2}{2Md^2}\left(\frac{1}{\nu^c D^C} + \left(\frac{\nu^G}{\nu^C}\right)^2 \frac{1}{\nu^G D^G}\right) \quad \text{(equ. 5)}$$

, where M is the mass of the membrane, Qc is the total charge of the graphene layer, and D is the diffusion constant, ν are the electron compressibilities of the gate or channel, respectively.

Scaling of the quality factor with temperature is found to be inverse, whereas the viscous damping is expected to scale with $\sqrt{T}$. Moreover, another possible loss mechanism based on the formation and breakage of surface bonds, termed the Velcro effect [26] is expected to create a temperature-independent loss rate. Finally, the electron decoherence is expected to lead to a linear relation between temperature and inverse quality factor, as observed in our experiments.

5.4 Impact of resonator breakage

The RF response of the resonators permits the extraction of device properties after suitable de-embedding. To gain inside into our device, we introduced a simplified model that accounts for the current gain in the oscillating graphene channel but also the reflections from mismatched input and parasitic capacitances.

$$|S_{21}| = \frac{R_{DS} \quad g}{C_{GS} R_C \sqrt{8}\pi f} \quad \text{(equ. 6)}$$

,where R_{DS} is the channel resistance, R_c is the contact resistance, C_{GS} is the gate capacitance and g is the transconductance.[27]

The transconductance of a resonating graphene channel can be expressed as

$$g = g_m\left[1 + \frac{V_g^2 \nu_{GS} \varepsilon_0}{0.735\sigma_A d\rho (2\pi f_r)^2 z_0^3}\left|\frac{1}{1 - \left(\frac{f}{f_r}\right)^2 + j\frac{1}{Q}\frac{f}{f_r}}\right|\right. \quad \text{(equ. 7)}$$

V_g is the gate voltage, $\nu_{GS}$is the input signal, z0 is the resonator amplitude, d is the membrane thickness, ρ is the membrane density, Q is the quality factor, and f_r is the resonance frequency. In this model, σ_A is the area fraction of the suspended membrane compared to the supported region.[28] We fit the equation and see an excellent agreement with experimental values.

Assuming all other variables are constant, we can estimate the change in area fraction of the resonators upon tensioning. Compared to the initial value, the area fraction decreases by 90% and 98% after straining to 0.2% and 0.5%, respectively. This result indicates that the large number of

parallel resonators in our device structure is a crucial feature to achieving high quality factors.

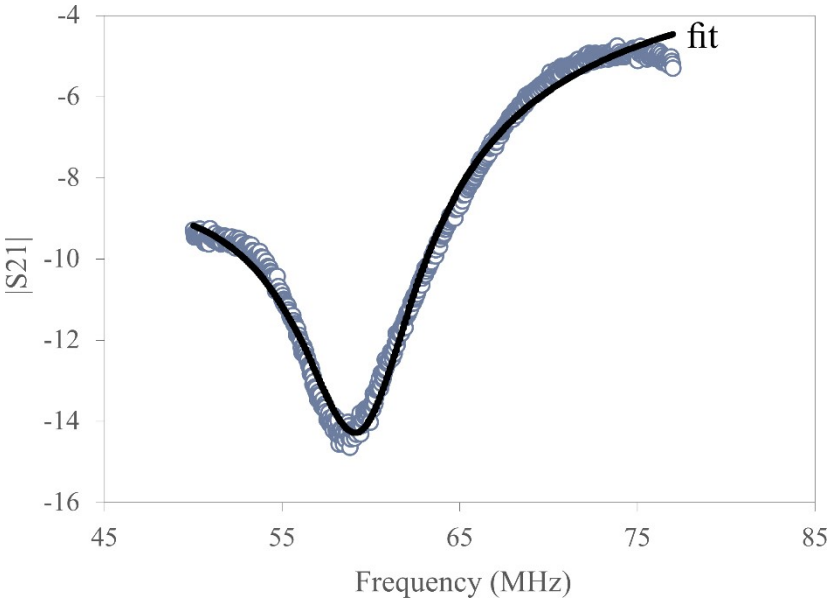

Figure S13 *Fit of |S21| frequency sweep to the model developed in the text, demonstrating good agreement*

6. Atomic force microscopy (AFM) Characterization of graphene membrane

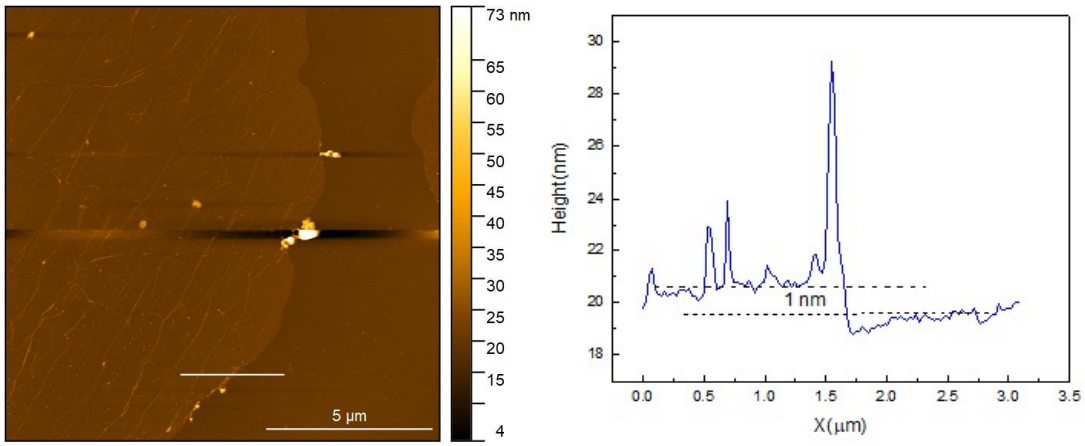

Figure S14 *The AFM image and its corresponding height profile confirming a thickness of 1 nm as expected for single-layer graphene..*

References

1. Moore, T. L.; Rodriguez-Lorenzo, L.; Hirsch, V.; Balog, S.; Urban, D.; Jud, C.; Rothen-Rutishauser, B.; Lattuada, M.; Petri-Fink, A., *Chemical Society Reviews* 2015,44,17, 6287-6305.
2. Mampallil, D.; Eral, H. B., *Advances in Colloid and Interface Science* 2018,252, 38-54.
3. Novoselov, K. S.; Geim, A. K.; Morozov, S. V.; Jiang, D.; Zhang, Y.; Dubonos, S. V.;

Grigorieva, I. V.; Firsov, A. A., *Science* 2004,306,5696, 666-669.
4. Oupeng, L.; Yuehang, X.; Yunqiu, W.; Yunchuan, G.; Yong, Z.; Ruimin, X.; Bo, Y. In *Compact radio frequency model of graphene resonant channel transistor*, 2012 IEEE/MTT-S International Microwave Symposium Digest, 17-22 June 2012; 2012; pp 1-3.
5. Weinstein, D.; Bhave, S. A., *Nano Letters* 2010,10,4, 1234-1237.
6. Fung, W. Y.; Dattoli, E. N.; Lu, W., *Applied Physics Letters* 2009,94,20, 203104.
7. Jun, S.; Huang, X.; Hone, J., *Electronics Letters* 2006,42,25, 1.
8. Jensen, K.; Girit, C.; Mickelson, W.; Zettl, A., *Physical Review Letters* 2006,96,21, 215503.
9. Chen, C.; Lee, S.; Deshpande, V. V.; Lee, G.-H.; Lekas, M.; Shepard, K.; Hone, J., *Nature nanotechnology* 2013,8,12, 923-927.
10. Fardindoost, S.; Mohammadi, S.; Sarvari, R.; Panahi, S. S.; Jokar, E., *Nanotechnology* 2013,24,13, 135201.
11. Kwon, J.; Choi, J.; Kim, K.; Sim, J.; Kim, J.; Kim, J., *IEEE transactions on magnetics* 2009,45,5, 2332-2335.
12. Chang, J.; Koh, K.; Min, B.-K.; Lee, S. J.; Kim, J.; Lin, L., *ACS Applied Materials & Interfaces* 2013,5,19, 9684-9690.
13. Vick, D.; Sauer, V.; Fraser, A.; Freeman, M.; Hiebert, W., *Journal of Micromechanics and Microengineering* 2010,20,10, 105005.
14. Rieger, J.; Faust, T.; Seitner, M. J.; Kotthaus, J. P.; Weig, E. M., *Applied Physics Letters* 2012,101,10.
15. Fung, W. Y.; Dattoli, E. N.; Lu, W., *Applied Physics Letters* 2009,94,20.
16. Ning, Z.; Shi, T.; Fu, M.; Guo, Y.; Wei, X.; Gao, S.; Chen, Q., *Nano letters* 2014,14,3, 1221-1227.
17. Verbridge, S. S.; Shapiro, D. F.; Craighead, H. G.; Parpia, J. M., *Nano Letters* 2007,7,6, 1728-1735.
18. Stiller, P. L.; Kugler, S.; Schmid, D. R.; Strunk, C.; Hüttel, A. K., *physica status solidi (b)* 2013,250,12, 2518-2522.
19. More, S.; Naik, A., *Journal of Micromechanics and Microengineering* 2021,31,4, 045015.
20. Zhang, X.; Makles, K.; Colombier, L.; Metten, D.; Majjad, H.; Verlot, P.; Berciaud, S., *Nature Communications* 2020,11,1, 5526.
21. Schmid, S.; Hierold, C., *Journal of Applied Physics* 2008,104,9.
22. Aoust, G.; Levy, R.; Bourgeteau, B.; Le Traon, O., *Sensors and Actuators A: Physical* 2015,230, 126-135.
23. Ko, J. H.; Jeong, J.; Choi, J.; Cho, M., *Applied Physics Letters* 2011,98,17.
24. Verbridge, S. S.; Parpia, J. M.; Reichenbach, R. B.; Bellan, L. M.; Craighead, H. G., *Journal of Applied Physics* 2006,99,12.
25. Sementilli, L.; Romero, E.; Bowen, W. P., *Advanced Functional Materials* 2022,32,3, 2105247.
26. Seoánez, C.; Guinea, F.; Castro Neto, A. H., *Physical Review B* 2007,76,12, 125427.
27. Niknejad, A. M., *Electromagnetics for high-speed analog and digital communication circuits*.

Cambridge University Press: 2007.
28. Xu, Y.; Li, O.; Xu, R. In *Graphene resonant channel transistor*, 2013 IEEE International Wireless Symposium (IWS), IEEE: 2013; pp 1-6.